Nanoscale

PAPER

View Article Online
View Journal | View Issue

Cite this: *Nanoscale*, 2024, **16**, 17442

Electron–phonon interactions at the topological edge states in single bilayer Bi(111)†

Enamul Haque, *[a,b] Yuefeng Yin*[a,b] and Nikhil V. Medhekar *[a,b]

Received 22nd May 2024,
Accepted 26th August 2024

DOI: 10.1039/d4nr02172j

rsc.li/nanoscale

An intriguing feature of two-dimensional topological insulators is the topologically protected electronic edge state, which allows one-way carrier transport without backscattering. Although this feature has strong potential applications in lossless electronics, the ideal behavior of the edge states may be fragile due to electron–phonon (e–ph) interactions at room temperatures. Using density functional perturbation theory calculations for single bilayer Bi(111) as a prototypical 2D topological insulator, we show that e–ph scattering can be a significant source of backscattering at the topological edge states. We also show that e–ph interactions strongly correlate to the dispersions of the electronic edge states. In particular, the e–ph interactions increase significantly with temperature and are much stronger at the nonlinearly dispersed edge states of native edges compared to the linearly dispersed edge states of passivated edges, causing a significant energy dissipation in the temperature range of 200–400 K. Overall, we argue that the e–ph interactions can be a crucial factor at finite temperatures in controlling the electronic transport at the topologically protected edge states.

Introduction

Two-dimensional (2D) topological insulators (TIs) exhibit various novel phenomena such as topologically protected conducting edge states embedded in an insulating bandgap,[2,3] quantum spin Hall (QSH) effect,[2,4] and superconductivity.[5,6] These properties have made 2D TIs an active area of research in condensed matter physics and materials science due to their potential applications in spintronics,[7–9] quantum computing,[10] and low-energy electronics.[11,12] From a practical viewpoint, interactions between electrons and phonons (e–ph interactions) play a critical role in the transport properties of metals,[13] semiconductors,[14] and 3D TIs,[15] and are expected to play a similar role in the transport properties of 2D TIs. Although the "spin-momentum locking"[12] enhances the spin current induced *via* the QSH effect, in practice the QSH effect often deviates from the ideal behavior due to e–ph scattering inherent at the edges at finite temperatures. For example, it has been suggested that both off-state and on-state current in a field-effect-transistor based on a 2D TI can exhibit significant uncertainties due to e–ph scattering.[16] A fundamental understanding of e–ph interactions at the edges of 2D TIs is critical for resolving this issue. However, current understanding of the e–ph interactions is limited only to the surface states of 3D TIs and insulating surfaces of 2D TIs.[1,17–21]

In the case of 3D TIs, experimental observations and theoretical calculations have shown that the e–ph interactions play a critical role in modifying and manipulating the topologically protected electronic surface states as well as the electronic transport.[18,22–24] Notably, the e–ph interactions can transform the topological phase into a normal insulating phase *via* electronic band renormalization.[25,26] Compared to the 3D TIs, the reduced dimensionality of 2D TIs can significantly modify vibrational states and enhance e–ph interactions in ultrathin 2D films. This has been demonstrated in a recent study which showed that ultrathin Bi(111) exhibits much stronger e–ph interactions compared to its bulk counterpart.[21] Analogously, it can be expected that e–ph interactions can be significantly enhanced at topologically protected 1D edges of 2D TIs. Also, the QSH in the 1D edge state is typically observed at low temperatures (*e.g.*, few mK for HgTe and InAs/GaSb quantum wells,[4,27] and up to 100 K for WTe_2 monolayer[28]), where e–ph interactions have minimal impact. Experiments on WTe_2 monolayers show that when the temperature is above 100 K, the e–ph interactions become a dominant effect in controlling topological semi-metallic to metallic phase transitions compared to the presence of defects and impurities even for very high purity samples.[29] Although the topology protects the (1D) edge state of a 2D TI from backscattering at low temperatures,

[a]*Department of Materials Science and Engineering, Monash University, Clayton, 3800 VIC, Australia. E-mail: enamul.haque@monash.edu, yuefeng.yin@monash.edu, nikhil.medhekar@monash.edu*
[b]*ARC Centre of Excellence in Future Low Energy Electronics Technologies (FLEET), Monash University, Clayton, 3800 VIC, Australia*

†Electronic supplementary information (ESI) available. See DOI: https://doi.org/10.1039/d4nr02172j

whether it still protects the edge states from the backscattering around room temperature remains unclear.

Here we use single bilayer Bi(111) (SBB) as a representative example of 2D TIs to investigate the impact of e–ph interactions at the topological edge states. SBB is a pure elemental 2D TI with robust edge states induced by a strong intrinsic spin–orbit coupling effect.[30,31] Using first principles density functional perturbation theory calculations, we show that e–ph scattering at the edge states of SBB can be an important source of backscattering and charge carrier decay at room temperatures. We also show that e–ph interactions strongly correlate with the character of the electronic band topology of 2D TIs. In particular, the e–ph scattering increases with temperature causing a subsequent dissipation of energy, which critically depends on the character of the electronic band topology. This study provides a direct quantification of the impact of the e–ph interactions on electronic transport at the topological edge states and suggests a potential way to minimize the impact of e–ph interactions on the carrier transport towards a dissipation-less transport at room temperature.

Results and discussion

We first investigate electronic and phononic structure, e–ph scattering and its impact on the electronic dispersions in SBB, as summarized in Fig. 1. Bismuth is a heavy element with a strong intrinsic spin–orbit coupling (SOC), which splits triply degenerate Bi 6p orbital into $p_{1/2}$ and $p_{3/2}$ orbitals in a fully relativistic sense (Fig. 1a). The 6p orbital leads to six doubly degenerate electronic bands in the vicinity of Fermi level (Fig. 1b). From the comparison of wavefunction parity of SBB

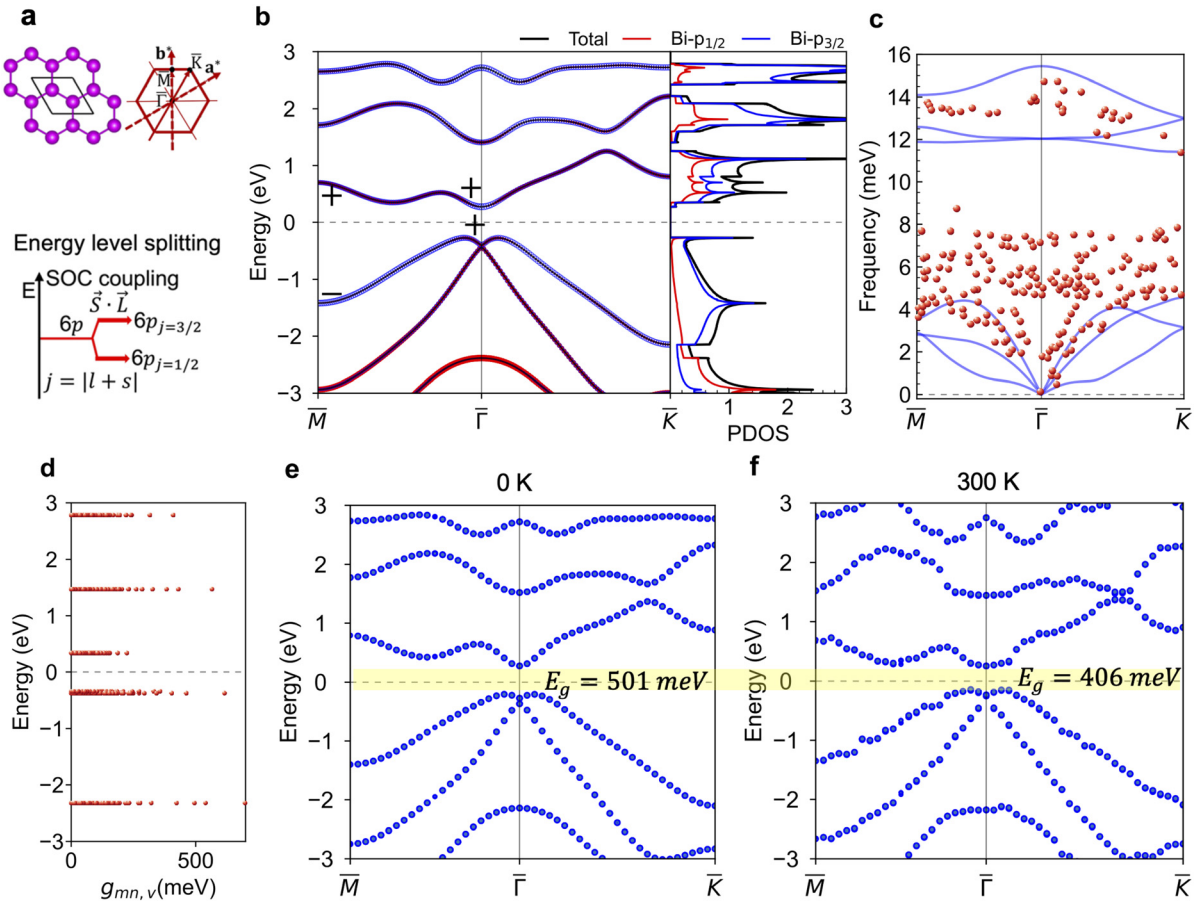

Fig. 1 Electronic and phononic structure, e–ph scattering and its impact on the electronic dispersions in single bilayer Bi(111). (a) Crystal structure of single bilayer Bi(111), with two Bi atoms per unit cell (lattice parameter 4.29 Å), along with its corresponding 2D Brillouin zone with high symmetry points. Also shown is the energy level splitting of triply degenerate p-orbital due to the fully relativistic spin–orbit coupling effect. Here, *L*, *S*, *j*, *l*, and *s* is the orbital angular momentum, spin angular momentum, total angular momentum, azimuthal quantum number and spin quantum number, respectively. (b) Fully relativistic electronic band structure and projected density of states at 0 K. Red and blue circles indicate the contributions of $p_{1/2}$ and $p_{3/2}$ states, respectively; + and – symbols indicate the parity of the corresponding bands. (c) Low energy phonon dispersions, calculated with spin–orbit coupling effect. The red spheres correspond to the experimental data (measured at 123 K for $\bar{M}-\bar{\Gamma}$ and at 103 K for $\bar{\Gamma}-\bar{K}$) of multi-layered Bi(111) obtained from ref. 1 as a reference. (d) Energy band resolved e–ph scattering matrix elements. (e and f) Electronic band structure calculated with density functional perturbation theory, taking into account e–ph scattering at 0 K and at 300 K. E_g denotes the band gap. In (b–f), the Fermi level is set to zero.

with and without SOC (Fig. S1†), it can be observed that the band inversion occurs (Fig. 1b) at the center of Brillouin zone (Fig. 1a). The $p_{3/2}$ states predominantly contribute to this band inversion, as seen from the projected band structure and density of states (Fig. 1b). Compared to the six doubly degenerate electronic bands, the SBB has six doubly degenerate phonon modes with three acoustic and three optical branches with no imaginary frequencies, confirming its dynamical stability (Fig. 1c). The calculated phonon dispersions are in excellent agreement with the available theoretical data of SBB.[19–21] As the experimental data on phonons in SBB is not yet available, we have plotted the experimental data (red circles in Fig. 1c) of multi-bilayers Bi(111) for a qualitative comparison.[1] Experiments on 40 nm thick few bilayers Bi(111) at 300 K report three optical phonons, where first two are doubly degenerate E_g modes at 8.5–8.6 meV and the third optical phonon is A_{1g} mode at the zone center at 11.6–11.9 meV.[32,33] Furthermore, these modes are blue-shifted with decreasing thickness and are qualitatively consistent with our calculated values of 11.9 and 15.2 meV for SBB, respectively.

To understand e–ph interactions in SBB, we first calculated band-resolved electron–phonon scattering matrix *via* density functional perturbation theory using the equation,

$$g_{mn,\nu}(\boldsymbol{k},\boldsymbol{q}) = \left(\frac{\hbar}{2M\omega_{\boldsymbol{q}\nu}}\right)^{1/2} \left\langle \psi_{m\boldsymbol{k}+\boldsymbol{q}} \middle| \partial_{\boldsymbol{q}\nu} V_{\mathrm{SCF}} \middle| \psi_{n\boldsymbol{k}} \right\rangle, \qquad (1)$$

where $\psi_{n\boldsymbol{k}}$ is the n^{th} Kohn–Sham wavefunction at wavevector $\boldsymbol{k}$ with energy eigenvalue $\varepsilon_{n\boldsymbol{k}}$, $\omega_{\boldsymbol{q}\nu}$ is the ν^{th} phonon frequency at phonon wavevector $\boldsymbol{q}$, and $\partial_{\boldsymbol{q}\nu}V_{\mathrm{SCF}}$ is the first order variation of Kohn–Sham self-consistent potential associated with the phonon wavevector $\boldsymbol{q}$.[34,35] The calculated values of the electron–phonon scattering matrix elements for SBB (greater than 500 meV, see Fig. 1d) illustrate that these phonon modes strongly interact with the electrons of $p_{1/2}$ and $p_{3/2}$ states. The e–ph interactions with matrix element values greater than 100 meV are generally considered to be strong.[36,37] As a comparison, the e–ph matrix element values in the range of 200–400 meV have been reported for graphene,[37] >600 meV for β-SnSe[36]. In particular, the topmost valence band has a stronger e–ph scattering than bottommost conduction band. These results suggest that the e–ph scattering can potentially modify the electronic band structure of SBB at finite temperatures. To investigate this further, we calculated electronic band structures at 0 K and 300 K, considering only e–ph scattering and neglecting any thermal expansion of the lattice. The electronic dispersion (see Fig. 1e) at 0 K is same as that of the normal DFT band structure with a band gap of 0.5 eV (Fig. 1b). As can be seen from Fig. 1f, the energy band dispersion at room temperature (300 K) is altered due to a strong electron–phonon scattering. In particular, the band spectrum is broadened over the momentum space and the VBM is pushed upward, reducing the bandgap by ~100 meV. These observations motivate us to explore whether the e–ph interactions can modify the edge bands in SBB and thereby impact the carrier transport at room temperatures. We also anticipate from these observations that the e–ph interactions in SBB cannot typically induce any structural phase transitions due to covalent nature of SBB, and furthermore, the structural stability of Bi(111) was experimentally verified up to 500 K.[38] It has been shown that in a covalent insulator (*e.g.*, SBB considered here), the perturbed energy of all phonons remains positive, *i.e.*, e–ph interactions are not strong enough to cause any phonon softening or structural distortions.[39]

Next we systematically investigate the edge electronic structures of SBB to obtain key essential insights into the physical origins of e–ph interactions at the edges. Free-standing SBB has topologically protected edge states (yellow circles in Fig. 2) inside the bandgap (blue circles). The edge states span over the whole 1D Brillouin zone ($\bar{M}$– $\bar{\Gamma}$ –$\bar{M}$) and form an isolated (from bulk conduction and valence bands, *i.e.*, blue circled bands) Dirac cone at the zone boundary ($\bar{M}$). However, these edge states in SBB nanoribbons with native edges do not possess a gapless Dirac cone at the zone center as in ideal 2D TIs.[3] For instance, the edge states near $\bar{\Gamma}$ of zigzag nanoribbon (Fig. 2a) are well separated from the adjacent bulk surface bands, and similar features are found in the armchair nanoribbon (Fig. 2b). The band dispersion of these edge states is nonlinear except in the upper part of the edge states (~0.2–0.5 eV above Fermi level for zigzag and ~0.4–0.6 eV above Fermi level for armchair). These band characteristics result from the presence of dangling bonds among Bi atoms in the native edge, and Bi $p_{3/2}$ states dominantly contribute to these nonlinear band features as shown in the projected density of states (Fig. 2e and f).

As shown in several previous studies,[40–43] we can utilize hydrogen to passivate the edge Bi atoms to remove the dangling bonds. As can be seen from Fig. 2e and f, the chemical passivation *via* hydrogen eliminates the dominance of Bi $p_{3/2}$ states and localizes the edge states at the zone center (Fig. 2c and d), making the dispersions similar to that of the edge states in HgTe/CdTe quantum well.[3] Consequently, the edge states (Fig. 2c and d) of hydrogen passivated edges become linear compared to those of the native edges. This change will potentially affect various types of scattering phenomena in the lattice. It should be noted that the shape of the edge bands in armchair nanoribbons (Fig. 2b and d) is slightly different compared to that reported in ref. 42 and 43 due to the differences in the width (see Fig. S2 in ESI†) of the nanoribbons[44] and the lattice parameters used. In our calculations, fully relaxed lattice parameters are in the range of 7.33–7.43 Å for the 2.3 nm wide armchair nanoribbon, while ref. 42 and 43 used the fixed value of 7.51 Å for a wider nanoribbon (see Table S1†). As we considered the energy-dependent electron–phonon scattering over the whole 1D BZ, these small differences in band shape as well as the gap do not affect our analysis of electron–phonon scattering at these edge states. More details on this can be found in the ESI.†

Now we focus on how e–ph interactions at the edges of SBB change with temperature and correlate with electronic dispersions. Since the passivation can alter the dispersion of the electronic edge states of SBB, it can also alter the phonon dis-

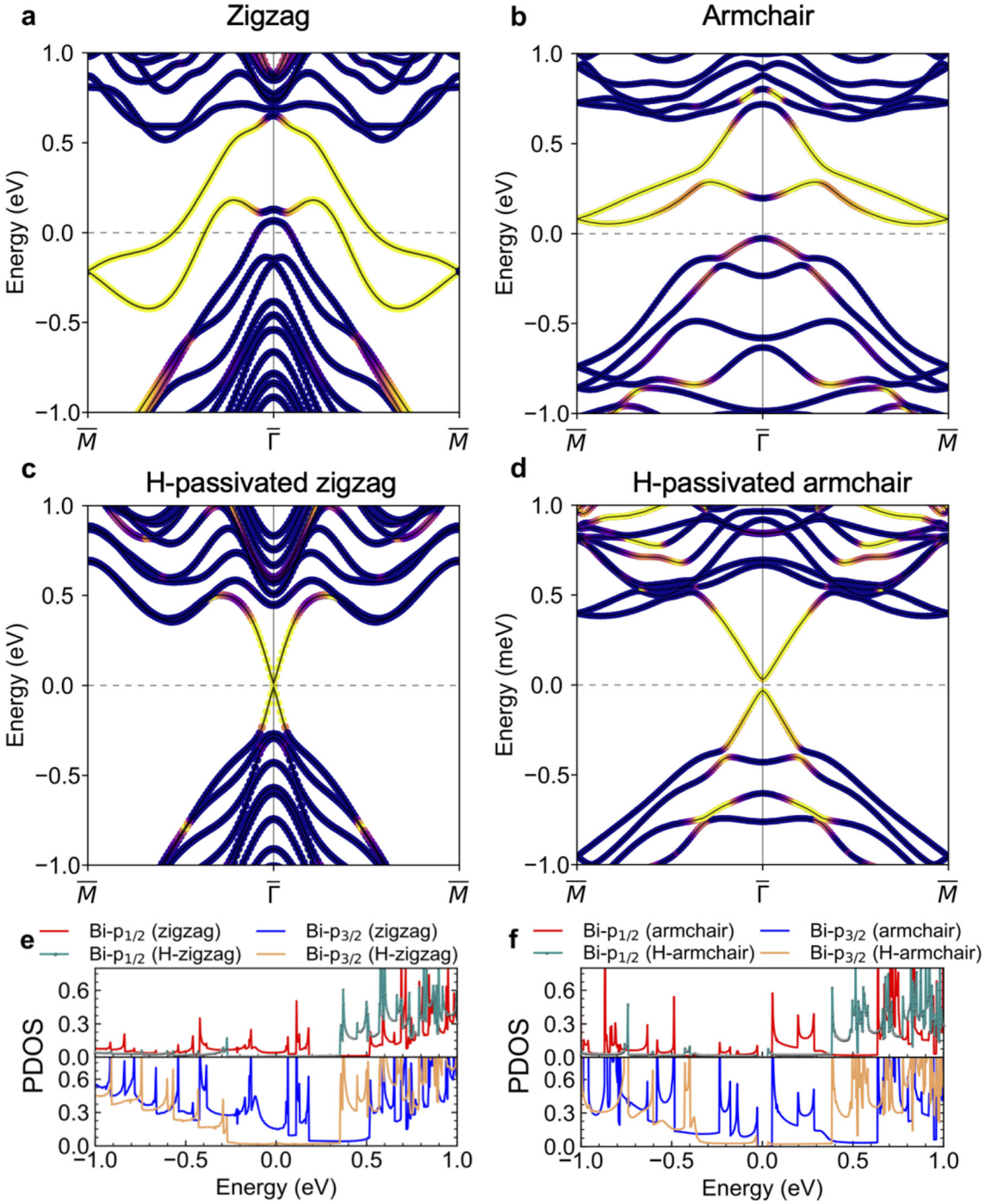

Fig. 2 Edge orientation dependent electronic dispersion showing the bulk and edge contributions in single bilayer Bi(111). (a–d) Edge projected electronic band structures for zigzag and armchair nanoribbons, unpassivated (a and b) and hydrogen-passivated (c and d). Yellow and blue circles indicate the contributions from the edge and the bulk, respectively. The dashed lines in each sub-figure indicate the Fermi level. (e and f) Projected densities of Bi $p_{1/2}$ and $p_{3/2}$ states for zigzag and armchair edges. The zigzag and armchair nanoribbons are 3.3 nm and 2.3 nm wide (Fig. S2†), respectively.

persions. Therefore, it is necessary to analyze the phonon dispersions of both SBB and its nanoribbons before proceeding to investigate e–ph interactions. Using density functional perturbation theory calculations, we obtained phonon dispersions for all the cases of SBB nanoribbons considered here. In these calculations, the acoustic sum with three translational invariances and one rotational invariance along the direction of the periodicity was applied by using the optimized correction of the dynamical matrix. We present the phonon dispersions of 1D edges in Fig. 3.

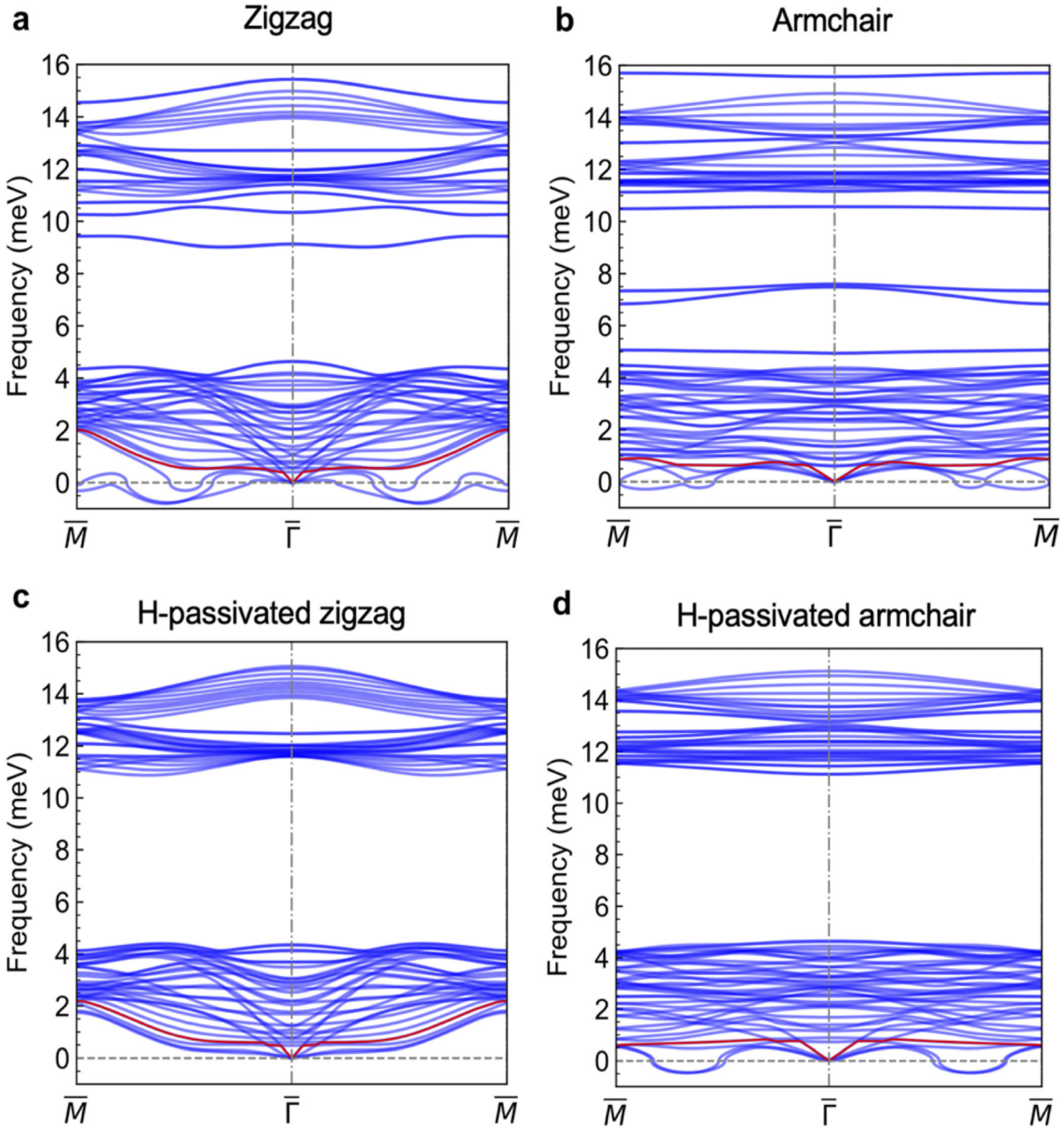

Fig. 3 Edge orientation dependent phononic dispersions in single bilayer Bi(111). Phonon dispersions obtained using density functional perturbation theory calculations for (a) zigzag nanoribbon, (b) armchair nanoribbon, (c) zigzag nanoribbon with H-passivation, and (d) armchair nanoribbon with H-passivation. The red-colored phonon band is the fourth acoustic mode for the rotational invariance along the periodic direction of the nanoribbon.

In the case of zigzag edge, the first three acoustic phonons are the in-phase vibrational modes (blue curves), while the fourth acoustic phonon (red curve) is induced due to the rotational symmetry along the periodic direction of the ribbon. Three acoustic modes of native, unpassivated zigzag edge are soft outside $\bar{\Gamma}$ (Fig. 3a), which may be attributed to internal stress along its plane despite the structure being fully relaxed.[45–47] Compared to the unpassivated zigzag edge, the phonon dispersions of passivated zigzag edge are significantly modified (see Fig. 3c). In particular, these dispersions do not contain any soft phonon modes. On the other hand, the phonon dispersions of armchair edges (Fig. 3b and d) have two soft modes regardless of the passivation and differ significantly compared to zigzag edges, denoting that the lattice vibrations depend significantly on the edge orientations. The existence of soft phonon modes in the phonon dispersions suggests dynamical instability (see ESI† for further details) near the high symmetry point $\bar{M}$ of the armchair edges.

We now discuss how the phonon modes interact with the electronic edge states at different temperatures. As mentioned earlier, the topological edge states are protected from the back-scattering induced by the small perturbation, for example, due

to the presence of nonmagnetic impurity. In this work, we assume that the e–ph interactions are the dominant source of backscattering and charge carrier decay, while neglecting any thermal expansion, any defects and impurities. Although the impurity and disorder effects can be significant compared to e–ph scattering at low temperature ($T \lesssim 100$ K), the e–ph interactions becomes dominant above 100 K over all other effects even in very high purity samples.[48]

The e–ph interactions mainly consist of two types: e–ph scattering and e–ph coupling. Among them, electron–phonon scattering is a dominant scattering process in metals, insulators, and semiconductors at finite temperatures and can significantly affect electronic transport.[13] The strength of the electron–phonon scattering can be characterized by measuring the carrier's scattering rate, which is inversely proportional to the relaxation time. Here we have used an averaging approach to calculate e–ph scattering using density functional perturbation theory, which is known to give accurate estimates of the scattering rates at temperatures above Debye temperature.[13,49,50] Incidentally, Bismuth has a low Debye temperature (112–114 K (ref. 51) for 3D and 76–92 K (ref. 52) for 2D) due to its heavier mass and low sound velocity. We calculated the relaxation times at the edge states by considering only e–ph scattering, by numerically solving the equation[53,54]

$$\begin{aligned}\tau^{-1}(\varepsilon,\mu,T) = \frac{2\pi\Omega}{g_s\hbar}\sum_{v}\{g_v^2(\varepsilon,\varepsilon+\bar{\omega}_v)[n(\bar{\omega}_v,T) \\ +f(\varepsilon+\bar{\omega}_v,\mu,T)]\rho(\varepsilon+\bar{\omega}_v) + g_v^2(\varepsilon,\varepsilon-\bar{\omega}_v) \\ \times[n(\bar{\omega}_v,T)+1-f(\varepsilon-\bar{\omega}_v,\mu,T)]\rho(\varepsilon-\bar{\omega}_v)\}.\end{aligned} \quad (2)$$

Here Ω, $\hbar$, and $\bar{\omega}_v$ are the primitive unit cell volume, the reduced Planck's constant, and the averaged phonon mode energy, respectively. g_v^2, $n(\bar{\omega}_v,T)$, T, $f(\varepsilon+\bar{\omega}_v,\mu,T)$, $g_s = 2$, and ρ stand for the averaged electron–phonon scattering matrix, the Bose–Einstein distribution function, the Fermi–Dirac distribution function, the spin degeneracy, the electron energy, and the electronic density of states (DOS) per unit energy and unit volume, respectively.

We present calculated e–ph scattering times and electrical conductivity for SBB as well as the zigzag and armchair nanoribbons in the temperature range of 200 K–400 K in Fig. 4. It should be noted that we explicitly considered the SOC effect in these calculations. At low temperature (200 K), small thermal broadening leads to a longer scattering time (inverse of linewidth) in the vicinity of Fermi level (Fig. 4(a–c)) *via* suppressing optical phonon scattering, as Pauli exclusion principle does not allow transition into filled electronic states for small thermal broadening.[55–57] Faraway from the Fermi level, the sharp fall of scattering time (Fig. 4a) indicates the increase in the available scattering phase space for electronic state transitions (*i.e.*, the number of available states to be scattered, see eqn (1)). Also, such change is directly related to the increase of density of states far away from the surface bandgap (Fig. 1b or Fig. 2e, f). However, the linewidths of 2D surface and 1D edge have a distinct feature in the vicinity of the Fermi level. In particular, the linewidth of linear edge state in 1D passivated edges gets much shorter inside the 2D surface bandgap compared to the nonlinear states (native, unpassivated edges) due to more restricted scattering phase space and lower density of states (Fig. 2(e and f)).

Increasing temperature to 300 K (or above) for a given energy, the thermal broadening becomes significant (as the maximum energy of the optical phonons in SBB is ≈16 meV (Fig. 1c, or Fig. 3)),[58] and the optical phonon scattering comes into play in the vicinity of Fermi level. This leads to a dramatic reduction of scattering time of the edge states in all cases (Fig. 4(b and c)), *i.e.*, a significant increase in e–ph scattering with temperature despite topological protections of the edge states. To the best of our knowledge, this is a first clear demonstration that e–ph scattering can indeed be a pivotal source of backscattering in the topological edge states at finite temperatures in a real material, as suggested earlier by quantum mechanical model developed for hypothetical systems.[56,57,59–61] This is further reflected in the calculated electrical conductivity values (Fig. 4(e and f)), suggesting that such source of backscattering can lead to a significant energy dissipation throughout the topological edge states at room temperature.

For a given temperature, we now discuss how electron–phonon scattering correlates with different type of electronic bands dispersions. In 2D SBB, the highly dispersive valence band has low density of states compared to the conduction bands (Fig. 1(b)). This leads to the longer relaxation time (τ) of holes than that of electrons, and τ peaks at around 0.25 eV (Fig. 4a), where the SOC effect induces a hat-like VBM of SBB (Fig. 1b). In contrast, the relaxation time of unpassivated zigzag edge (with nonlinear dispersion) is much shorter than that of SBB below 0.25 eV (Fig. 4b). At the upper regime (∼0.45 eV) of the edge states of zigzag edge, the relaxation time is approximately 10 fs at 200 K, which is higher than that at the lower regime (−0.3 to 0.4 eV) of the edge states. After passivation, the relaxation time of the edge states increases sharply. The lime-colored shaded areas in Fig. 4b highlight the energy region for the linear edge states. The sharp increase in carrier relaxation time of passivated zigzag edge indicates a dramatic reduction in e–ph collisions due to linear dispersion. The maximum relaxation time of the carriers at linearly dispersed edge states is over 20 times higher than that of bulk surface carriers, while it is more than 100 times higher than that of the carriers at the nonlinearly dispersed edge states. This shows that the e–ph scattering weakens as the band dispersion becomes linear.

To obtain a broader picture of whether the e–ph scattering is stronger at nonlinearly dispersed edge states, we also calculated the relaxation time at the edge states of armchair and passivated armchair edges, which have two soft acoustic phonon modes (Fig. 3b) compared to three soft phonon modes in zigzag edge (Fig. 3a). In the case of armchair edge, the relaxation time of the carriers at upper regime (∼0.5 eV) of the edge states is ∼40 fs at 200 K, which is significantly higher than that at the lower energy regime of the edge states. The relaxation time rises sharply at the edge states with a peak ∼0.5 eV and falls in the region of the surface carrier's contributions. In contrast to the native, unpassivated armchair edge,

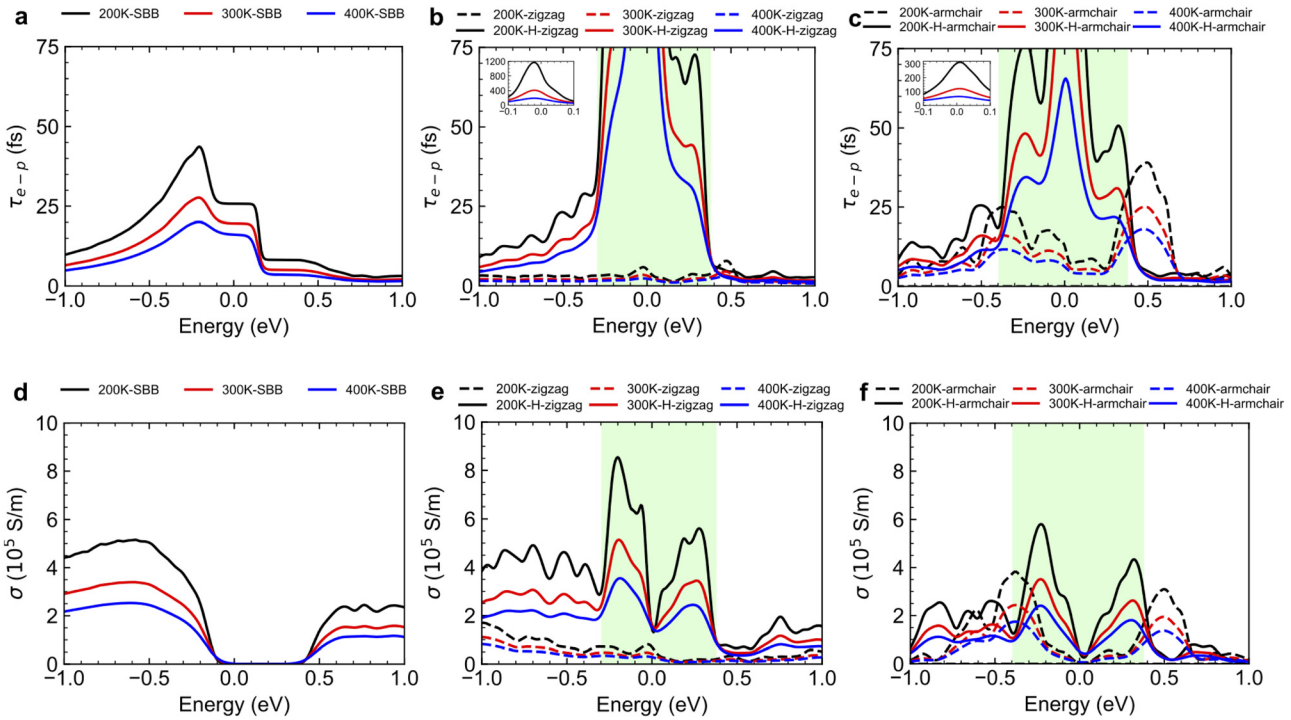

Fig. 4 Carrier relaxation times and electrical conductivity of 2D and 1D single bilayer Bi(111). (a) Temperature dependent relaxation time of 2D single bilayer Bi(111) as a function of the chemical potential. (b and c) Relaxation time as a function of chemical potential for different temperatures for unpassivated and passivated zigzag (b) and armchair (c) edges. The insets show the full-scale relaxation times near the Fermi energy. (d) Temperature dependent electrical conductivity of 2D single bilayer Bi(111) as a function of the chemical potential. (e and f) Electrical conductivity as a function of chemical potential for different temperatures for unpassivated and passivated zigzag (e) and armchair (f) edges. The Fermi level is set to zero in all cases. The lime-colored shaded area in (b, c and e, f) indicates the energy region for the linear edge states in the passivated nanoribbons.

the linearly dispersed edge states of passivated armchair edge lead to much longer relaxation time (Fig. 4c). The maximum relaxation time (inset figure) of carriers at linearly dispersed edge states is more than 60 times higher than the relaxation time of edge carriers at nonlinearly (lower regime ~0.2 eV) dispersed edge. This further confirms that the nonlinearly dispersed edge states of pristine SBB lead to a strong e–ph scattering around 200–400 K, while the e–ph scattering is weaker at the linearly dispersed states of the passivated SBB edges.

To place the results for e–ph scattering for 2D and 1D SBB presented in Fig. 4 in a broader context, we compare the calculated relaxation time of the linearly dispersed edge states of passivated zigzag and armchair edges of SBB with the available experimental data for other 2D materials. In the case of passivated SBB zigzag edge, the maximum relaxation time is 1.1 ps at 200 K, which is similar to the measured relaxation time 1.1 ps at a very low temperature of 1.5 K of the edge states of HgTe quantum well.[62] At these low temperatures, there will be no significant e–ph scattering at the edge states of HgTe, leading to such longer relaxation time of 1.1 ps. It is worth mentioning here that HgTe quantum-well exhibits QSH effect[4] and its edge states show an ideal dispersion, *i.e.*, linear dispersion.[40] Compared to passivated zigzag edge, the maximum relaxation time of the carriers at the linearly dispersed edge states of passivated armchair edge is 319 fs at 200 K, which falls within the range of measured relaxation time for massless fermions in graphene (250–450 fs (ref. 63)).

We now illustrate how e–ph scattering affects carrier transport by examining the changes in electrical conductivity. Our results indicate that e–ph scattering is weak at the linearly dispersed edge states of passivated zigzag and armchair edges, which is reflected in their high electrical conductivity (Fig. 4 (d–f)). Even within the negligibly small bandgap of the Dirac cone of passivated zigzag and armchair edges, their longer relaxation time results in very high electrical conductivity of ~10^5 S m^{-1}, exceeding that of any semiconductors. This suggests their potential application in low power electronic devices. For example, n-type (doped) Bi_2Te_3 has a maximum value of the electrical conductivity ~6.9×10^4 S m^{-1} at 300 K,[64] while the silicon and germanium have much lower electrical conductivity (<10^3 S m^{-1}).[65,66] Moreover, the lower electrical conductivity of the nonlinearly dispersed edge states indicates that a significant amount of energy can be dissipated throughout the edge states of pristine SBB due to e–ph scattering around 200–400 K. Thus, the enhanced linearity of edge states in passivated SBB edges plays a significant role in carrier transport, as e–ph scattering becomes weaker for linear band dispersions. The e–ph scattering and carrier transport notably differ in linearly and nonlinearly dispersed edge states because the linearly dispersed edge states have an ideal Dirac

Table 1 e–ph coupling constants (λ) for the 1D conducting edges of single bilayer Bi(111)

	λ
Zigzag	0.114
Passivated zigzag	0.105
Armchair	0.146
Passivated armchair	0.071

like dispersions which are fully protected from backscattering at low temperatures.[31] Aforementioned findings are physically significant because the e–ph scattering induces larger deterministic impact (depending on the linearity and nonlinearity of the edge states) on the carrier transport around room temperatures, *i.e.*, e–ph scattering significantly reduces electrical conductivity of the topologically protected edge states in SBB. Overall, these results suggest the importance of e–ph interactions in evaluating carrier transport and for designing ultralow energy electronic devices based on a 2D topological insulator. Furthermore, these results also point out that it is important to take into account factors such as presence of dangling bonds and nonlinearities in the edge states, as well as the magnitude of e–ph interactions in linearly dispersed edges.

As the edge states are conducting, the second type of e–ph interactions, *i.e.*, e–ph coupling, may also be present at the edge states. e–ph coupling, which involves the pairing of loosely bound electrons through phonons, is only present in metallic states. While the e–ph coupling itself does not badly affect electronic transport, e–ph scattering can significantly slow down the carrier transport. As we have shown how e–ph scattering varies with edge state dispersions, we next investigate how e–ph coupling operates in linearly and nonlinearly dispersed edge states. Table 1 shows the values of electron–phonon coupling constants for 1D SBB, calculated using density functional perturbation theory including the SOC effect (see ESI† for details). Here, the finite value of the λ indicates that e–ph coupling exists at all different types of edge states. In general, the coupling is stronger in the case native, unpassivated edges with nonlinear dispersion. The weak e–ph coupling at the linearly dispersed edge states of passivated zigzag and armchair edges is comparable to the e–ph coupling (in the range of 0.076–0.088) at the linearly dispersed surface states of 3D TI Bi_2Se_3, which is regarded one of the weakest e–ph coupling ever measured in any material.[67] As we demonstrated earlier that the e–ph scattering is negligibly weaker at the linearly dispersed edge states, this further supports the fact that the e–ph interactions are negligibly weak at the linearly dispersed edge states compared to the nonlinearly dispersed edge states of the pristine SBB.

Conclusions

Our study based on first-principles density functional perturbation theory calculations sheds light on the interplay between charge carriers and phonon dynamics at the edge states in 2D topological materials. Using the SBB as a representative example, we show that e–ph scattering can be a significant source of backscattering at temperatures around 300 K. We also show that such source backscattering can cause a significant charge carrier decay, *i.e.*, energy dissipation at the edge states. Furthermore, we find that e–ph interactions strongly depend on the character of electronic edge dispersion, *i.e.*, linear, and nonlinear. The e–ph interactions are negligibly weaker at the linear edge at low temperatures, ensuring long-lived quasiparticles in the linear edge state for dissipationless energy transport. Overall, our results quantitatively indicate that the e–ph interactions can be a pivotal factor in realizing lossless electronic transport—an ideal behavior dictated by the electronic band topology of SBB. Our in-depth investigation of the impact of e–ph interactions in 2D topological insulators provides invaluable physical insights to future research on device fabrications and technological developments in the field of ultralow energy electronics, spotlighting the importance of many-body physics in practical devices.

Methods

We used the plane wave (PW) pseudopotential method based on the density functional theory (DFT)[68] and density functional perturbation theory (DFPT) in Quantum ESPRESSO[35,69] to conduct the electronic structures and electron–phonon calculations. We adopted the GGA-PBE functional for the exchange–correlation term.[44] We used fully relativistic ultrasoft pseudopotential with 45 Ry cutoff energy for wave functions, 480 Ry cutoff energy for charge density, 0.035 Ry Gaussian smearing width, $16 \times 16 \times 1$ $\boldsymbol{k}$-point mesh, 881 $\boldsymbol{q}$-points, self-consistency convergence threshold of 10^{-7} Ry, phonon convergence threshold of 10^{-18} Ry, and potential mixing parameter of 0.2. For electronic structure calculations, we considered a denser $24 \times 24 \times 1$ $\boldsymbol{k}$-point mesh. For nanoribbons, we used the same parameters as above except $12 \times 1 \times 1$ and $1 \times 12 \times 1$ $\boldsymbol{k}$-point mesh, and 611 and 161 $\boldsymbol{q}$-points for or zigzag and armchair, respectively, along with self-consistency convergence of 10^{-10} Ry. We calculated finite-temperature band-structure by using the approach described in ref. 70. The average electron–phonon dynamical matrix, carrier lifetime, and electrical conductivity were computed by using EPAMLS[54] and BoltzTraP codes.[71] See ESI† for further computational details.

Author contributions

E. H. conceptualized this research, performed all calculations, analyzed all data, and wrote the manuscript. Y. Y. provided critical review and corrections to the manuscript. N. V. M. conceptualized this research, provided critical reviews and corrections, and supervised the project.

Data availability

All data are included in the manuscript and the raw data are available upon request to the corresponding author.

Conflicts of interest

There is no conflict of interest to declare.

Acknowledgements

Enamul Haque acknowledged the financial support from Monash University through Monash Graduate Scholarship (MGS) and Monash International Tuition Scholarship (MITS). All authors gratefully acknowledge the supercomputing support from the National Computational Infrastructure (NCI Australia) and Pawsey Supercomputing Research Centre. All authors acknowledge the support of the Australian Research Council's Centre of Excellence in Future Low-Energy Electronics Technologies (FLEET) (CE170100039).

References

1 A. Tamtögl, P. Kraus, M. Mayrhofer-Reinhartshuber, D. Campi, M. Bernasconi, G. Benedek and W. E. Ernst, *Phys. Rev. B: Condens. Matter Mater. Phys.*, 2013, **87**, 035410.
2 C. L. Kane and E. J. Mele, *Phys. Rev. Lett.*, 2005, **95**, 146802.
3 L. Kou, Y. Ma, Z. Sun, T. Heine and C. Chen, *J. Phys. Chem. Lett.*, 2017, **8**, 1905–1919.
4 M. Konig, S. Wiedmann, C. Brune, A. Roth, H. Buhmann, L. W. Molenkamp, X.-L. Qi and S.-C. Zhang, *Science*, 2007, **318**, 766–770.
5 H.-H. Sun, M.-X. Wang, F. Zhu, G.-Y. Wang, H.-Y. Ma, Z.-A. Xu, Q. Liao, Y. Lu, C.-L. Gao, Y.-Y. Li, C. Liu, D. Qian, D. Guan and J.-F Jia, *Nano Lett.*, 2017, **17**, 3035–3039.
6 C. Zhao, L. Li, L. Zhang, J. Qin, H. Chen, B. Xia, B. Yang, H. Zheng, S. Wang, C. Liu, Y. Li, D. Guan, P. Cui, Z. Zhang and J. Jia, *Phys. Rev. Lett.*, 2022, **128**, 206802.
7 S.-H. Yang, R. Naaman, Y. Paltiel and S. S. Parkin, *Nat. Rev. Phys.*, 2021, **3**, 328–343.
8 D. Pesin and A. H. MacDonald, *Nat. Mater.*, 2012, **11**, 409–416.
9 A. Shitade and G. Tatara, *Phys. Rev. B*, 2022, **105**, L201202.
10 X.-L. Qi and S.-C. Zhang, *Rev. Mod. Phys.*, 2011, **83**, 1057.
11 C. X. Trang, Q. Li, Y. Yin, J. Hwang, G. Akhgar, I. Di Bernardo, A. Grubisic-Cabo, A. Tadich, M. S. Fuhrer, S.-K. Mo, N. V. Medhekar and M. T. Edmonds, *ACS Nano*, 2021, **15**, 13444–13452.
12 M. Z. Hasan and C. L. Kane, *Rev. Mod. Phys.*, 2010, **82**, 3045.
13 F. Giustino, *Rev. Mod. Phys.*, 2017, **89**, 015003.
14 C. Zhang and Y. Liu, *Phys. Rev. B*, 2022, **106**, 115423.
15 D. Kim, Q. Li, P. Syers, N. P. Butch, J. Paglione, S. D. Sarma and M. S. Fuhrer, *Phys. Rev. Lett.*, 2012, **109**, 166801.
16 W. G. Vandenberghe and M. V. Fischetti, *Nat. Commun.*, 2017, **8**, 1–8.
17 J. Choe, D. Lujan, M. Rodriguez-Vega, Z. Ye, A. Leonardo, J. Quan, T. N. Nunley, L.-J. Chang, S.-F. Lee, J. Yan, G. A. Fiete, R. He and X. Li, *Nano Lett.*, 2021, **21**, 6139–6145.
18 X. Zhu, L. Santos, C. Howard, R. Sankar, F. Chou, C. Chamon and M. El-Batanouny, *Phys. Rev. Lett.*, 2012, **108**, 185501.
19 A. Tamtögl, M. Mayrhofer-Reinhartshuber, N. Balak, W. Ernst and K.-H. Rieder, *J. Phys.: Condens. Matter*, 2010, **22**, 304019.
20 V. Chis, G. Benedek, P. M. Echenique and E. V. Chulkov, *Phys. Rev. B: Condens. Matter Mater. Phys.*, 2013, **87**, 075412.
21 M. A. Ortigoza, I. Y. Sklyadneva, R. Heid, E. V. Chulkov, T. Rahman, K.-P. Bohnen and P. M. Echenique, *Phys. Rev. B: Condens. Matter Mater. Phys.*, 2014, **90**, 195438.
22 J. A. Sobota, S.-L. Yang, D. Leuenberger, A. F. Kemper, J. G. Analytis, I. R. Fisher, P. S. Kirchmann, T. P. Devereaux and Z.-X. Shen, *Phys. Rev. Lett.*, 2014, **113**, 157401.
23 H. Pal, V. Yudson and D. Maslov, *Phys. Rev. B: Condens. Matter Mater. Phys.*, 2012, **85**, 085439.
24 V. Parente, A. Tagliacozzo, F. Von Oppen and F. Guinea, *Phys. Rev. B: Condens. Matter Mater. Phys.*, 2013, **88**, 075432.
25 I. Garate, *Phys. Rev. Lett.*, 2013, **110**, 046402.
26 K. Saha and I. Garate, *Phys. Rev. B: Condens. Matter Mater. Phys.*, 2014, **89**, 205103.
27 I. Knez, R.-R. Du and G. Sullivan, *Phys. Rev. Lett.*, 2011, **107**, 136603.
28 S. Wu, V. Fatemi, Q. D. Gibson, K. Watanabe, T. Taniguchi, R. J. Cava and P. Jarillo-Herrero, *Science*, 2018, **359**, 76–79.
29 R. Jing, Y. Shao, Z. Fei, C. F. B. Lo, R. A. Vitalone, F. L. Ruta, J. Staunton, W. J.-C. Zheng, A. S. Mcleod, Z. Sun, B.-Y. Jiang, X. Chen, M. M. Fogler, A. J. Millis, M. Liu, D. H. Cobden, X. Xu and D. N. Basov, *Nat. Commun.*, 2021, **12**, 5594.
30 M. Wada, S. Murakami, F. Freimuth and G. Bihlmayer, *Phys. Rev. B: Condens. Matter Mater. Phys.*, 2011, **83**, 121310.
31 F. Yang, L. Miao, Z. Wang, M.-Y. Yao, F. Zhu, Y. Song, M.-X. Wang, J.-P. Xu, A. V. Fedorov, Z. Sun, G. B. Zhang, C. Liu, F. Liu, D. Qian, C. L. Gao and J.-F. Jia, *Phys. Rev. Lett.*, 2012, **109**, 016801.
32 C. Rodríguez-Fernández, K. Akius, M. M. de Lima, A. Cantarero, J. M. van Ruitenbeek and C. Sabater, *Mater. Sci. Eng., B*, 2021, **270**, 115240.
33 E. Haro-Poniatowski, M. Jouanne, J. Morhange, M. Kanehisa, R. Serna and C. N. Afonso, *Phys. Rev. B: Condens. Matter Mater. Phys.*, 1999, **60**, 10080.
34 S. Baroni, P. Giannozzi and A. Testa, *Phys. Rev. Lett.*, 1987, **58**, 1861.
35 P. Giannozzi, S. Baroni, N. Bonini, M. Calandra, R. Car, C. Cavazzoni, D. Ceresoli, G. L. Chiarotti, M. Cococcioni, I. Dabo, A. D. Corso, S. D. Gironcoli, S. Fabris, G. Fratesi, R. Gebauer, U. Gerstmann, C. Gougoussis, A. Kokalj, M. Lazzeri, L. Martin-Samos, N. Marzari, F. Mauri, R. Mazzarello, S. Paolini, A. Pasquarello, L. Paulatto, C. Sbraccia, S. Scandolo, G. Sclauzero, A. P. Seitsonen, A. Smogunov, P. Umari and R. M. Wentzcovitch, *J. Phys.: Condens. Matter*, 2009, **21**, 395502.

36 W. Zhou, Y. Dai, T.-H. Liu and R. Yang, *Mater. Today Phys.*, 2022, **22**, 100592.
37 K. M. Borysenko, J. T. Mullen, E. Barry, S. Paul, Y. G. Semenov, J. Zavada, M. B. Nardelli and K. W. Kim, *Phys. Rev. B: Condens. Matter Mater. Phys.*, 2010, **81**, 121412.
38 M. Jankowski, D. Kamiński, K. Vergeer, M. Mirolo, F. Carla, G. Rijnders and T. R. Bollmann, *Nanotechnology*, 2017, **28**, 155602.
39 T. Riste, *Electron-phonon interactions and phase transitions*, Springer Science & Business Media, 2013.
40 S. S. Krishtopenko and F. Teppe, *Phys. Rev. B*, 2018, **97**, 165408.
41 Z. Wang, L. Chen and F. Liu, *Nano Lett.*, 2014, **14**, 2879–2883.
42 X. Li, H. Liu, H. Jiang, F. Wang and J. Feng, *Phys. Rev. B: Condens. Matter Mater. Phys.*, 2014, **90**, 165412.
43 K.-H. Jin and S.-H. Jhi, *Phys. Chem. Chem. Phys.*, 2016, **18**, 8637–8642.
44 J. P. Perdew, K. Burke and M. Ernzerhof, *Phys. Rev. Lett.*, 1996, **77**, 3865.
45 V. Shenoy, C. Reddy, A. Ramasubramaniam and Y. Zhang, *Phys. Rev. Lett.*, 2008, **101**, 245501.
46 Z. W. Tan, J.-S. Wang and C. K. Gan, *Nano Lett.*, 2011, **11**, 214–219.
47 R. Gillen, M. Mohr, C. Thomsen and J. Maultzsch, *Phys. Rev. B: Condens. Matter Mater. Phys.*, 2009, **80**, 155418.
48 S. Giraud, A. Kundu and R. Egger, *Phys. Rev. B: Condens. Matter Mater. Phys.*, 2012, **85**, 035441.
49 A. M. Ganose, J. Park, A. Faghaninia, R. Woods-Robinson, K. A. Persson and A. Jain, *Nat. Commun.*, 2021, **12**, 2222.
50 L. Cheng, C. Zhang and Y. Liu, *Phys. Rev. Lett.*, 2020, **125**, 177701.
51 P. Fischer, I. Sosnowska and M. Szymanski, *J. Phys. C: Solid State Phys.*, 1978, **11**, 1043.
52 M. Mayrhofer-Reinhartshuber, A. Tamtögl, P. Kraus, K.-H. Rieder and W. Ernst, *J. Phys.: Condens. Matter*, 2012, **24**, 104008.
53 W. Li, *Phys. Rev. B: Condens. Matter Mater. Phys.*, 2015, **92**, 075405.
54 S. Bang, J. Kim, D. Wee, G. Samsonidze and B. Kozinsky, *Mater. Today Phys.*, 2018, **6**, 22–30.
55 W.-K. Tse and S. D. Sarma, *Phys. Rev. Lett.*, 2007, **99**, 236802.
56 K. Dorn, A. De Martino and R. Egger, *Phys. Rev. B*, 2020, **101**, 045402.
57 J. C. Budich, F. Dolcini, P. Recher and B. Trauzettel, *Phys. Rev. Lett.*, 2012, **108**, 086602.
58 Z. Tian, K. Esfarjani, J. Shiomi, A. S. Henry and G. Chen, *Appl. Phys. Lett.*, 2011, **99**, 053122.
59 H. Liu, H. Jiang, Q.-F. Sun and X. Xie, *Phys. Rev. Lett.*, 2014, **113**, 046805.
60 G. Cho, T. Dekorsy, H. Bakker, R. Hövel and H. Kurz, *Phys. Rev. Lett.*, 1996, **77**, 4062.
61 S. Groenendijk, G. Dolcetto and T. L. Schmidt, *Phys. Rev. B*, 2018, **97**, 241406.
62 V. Daumer, I. Golombek, M. Gbordzoe, E. Novik, V. Hock, C. Becker, H. Buhmann and L. Molenkamp, *Appl. Phys. Lett.*, 2003, **83**, 1376–1378.
63 W. Choi, H. Nishiyama, Y. Ogawa, Y. Ueno, K. Furukawa, T. Takeuchi, Y. Tsutsui, T. Sakurai and S. Seki, *Adv. Opt. Mater.*, 2018, **6**, 1701402.
64 S. Byun, J. Cha, C. Zhou, Y. K. Lee, H. Lee, S. H. Park, W. B. Lee and I. Chung, *J. Solid State Chem.*, 2019, **269**, 396–400.
65 A. Hoffmann, K. Reuschel and H. Rupprecht, *J. Phys. Chem. Solids*, 1959, **11**, 284–287.
66 G. Yang, K. Kooi, G. Wang, H. Mei, Y. Li and D. Mei, *Appl. Phys. A*, 2018, **124**, 1–8.
67 Z.-H. Pan, A. Fedorov, D. Gardner, Y. S. Lee, S. Chu and T. Valla, *Phys. Rev. Lett.*, 2012, **108**, 187001.
68 P. Hohenberg and W. Kohn, *Phys. Rev.*, 1964, **136**, B864.
69 P. Giannozzi, O. Baseggio, P. Bonfà, D. Brunato, R. Car, I. Carnimeo, C. Cavazzoni, S. De Gironcoli, P. Delugas, F. Ferrari Ruffino, A. Ferretti, N. Marzari, I. Timrov, A. Urru and S. Baroni, *J. Chem. Phys.*, 2020, **152**, 154105.
70 M. Zacharias and F. Giustino, *Phys. Rev. Res.*, 2020, **2**, 013357.
71 G. K. Madsen and D. J. Singh, *Comput. Phys. Commun.*, 2006, **175**, 67–71.